A Coefficient of Variation Based Image Selective Segmentation Model Using Active Contours

Noor Badshah[*], Ke Chen[†], Haider Ali and Ghulam Murtaza [‡]

Abstract

Most image segmentation techniques are efficient to segment images with prominent edges, but are less so for some challenging images with low frequencies and with overlapping regions of homogeneous intensities. In our recent work we proposed an effective model of selective segmentation which works well for many examples except these challenging images. In this paper we propose a new model using the coefficient of variation as a fidelity term. Test results show that the new model performs much better than previous works in successfully segmenting the challenging images.

Keywords. Segmentation, Coefficient of Variation (CoV), Level Set, Functional Minimization, Total Variation (TV).

1 Introduction

In image segmentation, the main issue is to extract features according to a given criterion [3, 5, 6, 10, 11, 13, 15]. There exist two important categories of methods. The first category refers to edge-based methods. Through the seminal work of [5, 13, 8, 20], active contours have proven their effectiveness for such a task. The general idea behind an active contours model is to apply partial differential equations (PDEs) to deform a curve towards the boundaries of the object of interest. In these methods, the contour is driven towards image edges. For edge detection, most models use an edge detector function which depends on the gradient of a given image [3, 10, 11]. In contrast, the second category contains region-based methods. Among region based active contour models, we find minimum description length criteria [14], region growing and emerging [2], Mumford-Shah functional minimization [18] and watershed algorithms [24] as examples. Let $z(x, y)$ be a given image defined on a rectangular domain Ω. Mumford and Shah (MS) [18] proposed the general model:

$$\min_{u,\Gamma} F(u,\Gamma) = \mu.length(\Gamma) + \lambda \int_{\Omega} |z-u|^2 dx + \int_{\Omega\setminus\Gamma} |\nabla u|^2 dx.$$

[*]Department of Basic Sciences, UET Peshawar, Pakistan. Email: noor2k@gmail.com

[†]Centre for Mathematical Imaging Techniques and Department of Mathematical Sciences, The University of Liverpool, United Kingdom. Email: k.chen@liverpool.ac.uk / url: www.liv.ac.uk/cmit (Corresponding author)

[‡]Department of Basic Sciences, UET Peshawar, Pakistan.

to automatically find the edge Γ of z by a piecewise smooth function u. The Chan-Vese (CV) [6] model is a special case of the piecewise constant MS model when restricted to only two phases. Since the CV model is not based on the gradient of the image $z(x, y)$ for the stopping process, it can detect contours both with and without gradients. The CV active contour model uses the energy minimization functional given by:

$$F(c_1, c_2, \Gamma) = \mu.length(\Gamma) + \lambda_1 \int_{inside(\Gamma)} |z - c_1|^2 dxdy + \lambda_2 \int_{outside(\Gamma)} |z - c_2|^2 dxdy,$$

where z is a given image, Γ is an unknown boundary, c_1 and c_2 are constants depending on Γ and representing the average value of z inside and outside of Γ respectively.

The above categories of segmentation models are global because all global features are to be segmented. Although they are useful, however, in certain segmentation problems we need to segment a particular object and not all objects in it. Thus selective segmentation is a task in which an object/region of interest is detected, given additional information of geometric constraints in the form of list of points near the object/region.

In our recent work [3] we proposed a mixed model of edge-based and region-based methods, based on the work of [10, 11, 6] and [6]. There we achieved more robustness for noisy images than previous work. However, this old model [3] can produce spurious objects i.e. fails the selection in some cases. Now we equip our model with a new type of fidelity term that can work better even when edges are not prominent or an image has overlapping regions with almost homogeneous intensities. This fidelity term is based on coefficient of variation. Our experimental results ensure the better performance of this new type of fidelity term based model than the old one.

This paper is organized in the following way. Section 2 contains a review of the Badshah-Chen model [3]. In Section 3 we present our proposed new model of minimization and derive the Euler-Lagrange equation. In Section 4 we describe a semi-implicit method and an additive operator splitting (AOS) method for solving the PDE. In Section 5 we give some experimental results.

2 The Badshah-Chen Model

To segment a given image z or find the boundary Γ of a desirable feature, the Badshah and Chen (BC) model [3] solves

$$\min_{c_1, c_2, \Gamma} F(\Gamma, c_1, c_2)$$

where

$$\begin{aligned} F(\Gamma, c_1, c_2) &= \mu \int_\Gamma d(x, y) g(|\nabla z|) ds \\ &+ \lambda_1 \int_{outside(\Gamma)} (z - c_1)^2 dxdy + \lambda_2 \int_{inside(\Gamma)} (z - c_2)^2 dxdy \end{aligned} \tag{1}$$

and μ, λ_1 and λ_2 are constants and are used for assigning different weights, c_1 and c_2 are the mean intensities outside and inside a contour Γ respectively. The distance function $d(x, y)$ is define in [11] as

$$d(x,y) = \prod_{i=1}^{m} \left(1 - e^{-\frac{(x-x_i)^2}{2\sigma^2}} e^{-\frac{(y-y_i)^2}{2\sigma^2}}\right), \qquad \forall (x,y) \in \Omega,$$

where the marker set

$$\mathcal{A} = \{(x_i, y_i) : i = 1, 2, 3, ..., m\}$$

are the given geometrical constraints and we wish to detect the boundary of an interested object near $\mathcal{A}$. Intuitionally it is clear that in the neighborhood of $\mathcal{A}$, $d \approx 0$.

The function $g(|\nabla z|)$ is called as an edge detector function and the following one is a popular choice

$$g(|\nabla z|) = \frac{1}{1 + |\nabla z|^2}$$

but there exist many other choices. Since edge is the portion of an image where there is a sudden change in the intensity function, hence the value of the function $|\nabla z|^2$ is large at the pixels which belongs to edge. Consequently, $g(|\nabla z|) \simeq 0$ near an edge.

The first term of the Badshah-Chen model is the $\int_\Gamma d(x,y) g(|\nabla z|) ds$ similar to [10, 11]. The aim was to find the unknown boundary curve Γ by minimizing their proposed functional. Since this model depends on edge detector function which uses gradient information and this causes mal-functioning of the model in noisy images or in images with fuzzy or discrete edges. Isotropic Gaussian smoothing is necessary to smooth z but unfortunately it also smooth the edges. So the idea of geodesic active contours alone is not sufficient.

To empower this model to work in noisy images, region information are also used by adding $\lambda_1 \int_{outside(\Gamma)} (z - c_1)^2 dxdy + \lambda_2 \int_{inside(\Gamma)} (z - c_2)^2 dxdy$ with edge information to form the remaining 2 terms of the BC model. These terms belong to the CV model proposed in [6]. In this way the CV model and its advantages are utilized in the BC model.

Application of a level set formulation [19, 20, 22] enables us to get the implicit representation of the boundary, interior and exterior regions of the object of interest in a given image. Let us denote the exterior of Γ by Ω^+ and interior by Ω^-. If $\phi : \Omega \to \mathbb{R}$, a Lipchitz continuous function, is a level set function, then

$$\begin{aligned} \Gamma &= \{(x,y) : \phi(x,y) = 0\}, \\ \Omega^+ &= \{x,y) : \phi(x,y) > 0\}, \quad \Omega^- = \{(x,y) : \phi(x,y) < 0\}. \end{aligned}$$

Further, the quantities in equation (1) can be reformulated by

$$length\{\Gamma\} = \int_\Omega |\nabla H(\phi)| = \int_\Omega \delta(\phi) |\nabla \phi| dxdy,$$

$$\int_{outside(\Gamma)} |z-c_1|^2 dx = \int_{\Omega} |z-c_1|^2 H(\phi) dxdy,$$
$$\int_{inside(\Gamma)} |z-c_2|^2 dx = \int_{\Omega} |z-c_2|^2 (1-H(\phi)) dxdy.$$

where the one dimensional Heaviside and Dirac delta functions

$$H(x) = \begin{cases} 1 & \text{if } x \geq 0 \\ 0 & \text{if } x < 0 \end{cases} \qquad \text{and} \qquad \delta(x) = H'(x)$$

will be respectively replaced by regularized versions [6, 7, 19]

$$H_\epsilon(w) = \frac{1}{2}\Big(1 + \frac{2}{\pi}\arctan(\frac{w}{\epsilon})\Big), \qquad \delta_\epsilon(w) = H'_\epsilon(w) = \frac{\epsilon}{\pi(\epsilon^2 + w^2)}.$$

Thus equation (1) becomes

$$\begin{aligned} F_\epsilon(\phi, c_1, c_2) &= \mu \int_\Omega d(x,y) g(|\nabla z|) \delta_\epsilon(\phi) |\nabla \phi| dxdy + \lambda_1 \int_\Omega |z(x,y) - c_1|^2 H_\epsilon(\phi) dxdy \\ &+ \lambda_2 \int_\Omega |z(x,y) - c_2|^2 (1 - H_\epsilon(\phi)) dxdy. \end{aligned}$$

Keeping ϕ fixed and minimizing $F_\epsilon(\phi, c_1, c_2)$ with respect to c_1 and c_2, we have

$$c_1(\phi) = \frac{\int_\Omega z(x,y) H_\epsilon(\phi) dxdy}{\int_\Omega H_\epsilon(\phi) dxdy}, \text{ and } \quad c_2(\phi) = \frac{\int_\Omega z(x,y)(1 - H_\epsilon(\phi)) dxdy}{\int_\Omega (1 - H_\epsilon(\phi)) dxdy},$$

assuming that the curve has a non-empty exterior and non-empty interior in Ω. Now keeping c_1, c_2 fixed and minimizing F_ϵ with respect to ϕ yields the following Euler-Lagrange equation for ϕ:

$$\begin{cases} \delta_\epsilon(\phi)\Big[\mu \text{div}\Big(G(x,y)\frac{\nabla\phi}{|\nabla\phi|}\Big) \\ \qquad -\lambda_1(z(x,y) - c_1)^2 + \lambda_2(z(x,y) - c_2)^2\Big] = 0 \quad \text{in } \Omega, \\ \dfrac{G(x,y)\delta_\epsilon(\phi)}{|\nabla\phi|}\dfrac{\partial\phi}{\partial\vec{n}} = 0 \qquad\qquad\qquad\qquad \text{on } \partial\Omega, \end{cases} \tag{2}$$

where $G(x,y) = d(x,y)g(|\nabla z|)$, $\vec{n}$ is the unit exterior normal to the boundary $\partial\Omega$, and $\dfrac{\partial\phi}{\partial\vec{n}}$ is the normal derivative of ϕ at the boundary.

The above PDE may be considered as a steady state form of the evolution equation:

$$\frac{\partial\phi}{\partial t} = \delta_\epsilon(\phi)\Big[\mu\nabla.\Big(G(x,y)\frac{\nabla\phi}{|\nabla\phi|}\Big) - \lambda_1(z - c_1)^2 + \lambda_2(z - c_2)^2\Big], \quad in\ \Omega \tag{3}$$

where $\phi(t,x,y) = \phi_0(x,y)$ in Ω. For robustness and iteration initialization, a balloon term [11], $\alpha G(x,y)|\nabla\phi|$, was added, where α is constant. To solve the above evolution equation, an additive operator splitting method (AOS) was used [25, 16].

Although we have shown in [3] that this model is more robust than the existing models, however there are images where the above BC model will fail, in particular, MRI and CT images with fuzzy edges, unilluminated organs and overlapping homogeneous regions.

Since the BC model (1) involves the fidelity term or region detector $\int |z-c_1|^2 dxdy + \int |z-c_2|^2 dxdy$ taken from CV model [6], it not only carries its advantages to BC model but also inherits its weaknesses of a CV model. Experimental results showed that the BC model does not work efficiently while dealing with some tough images due to detection of spurious objects. For the detection of low contrast, unilluminated and overlapping homogeneous regions better region detectors are required.

3 Coefficient of Variation Equipped Selective Model

Based on the concept of coefficient of variation (CoV) [1, 17], we introduce a new type of fidelity term given by,

$$\lambda_1 \int_{outside(\Gamma)} \frac{(z-c_1)^2}{c_1^2} dxdy + \lambda_2 \int_{inside(\Gamma)} \frac{(z-c_2)^2}{c_2^2} dxdy.$$

Thus we propose the following model, to be denoted by CSM:

$$\min_{\Gamma, c_1, c_2} F(\Gamma, c_1, c_2)$$

where

$$F(\Gamma, c_1, c_2) = \mu \int_{\Gamma} d(x,y) g(|\nabla z|) ds + \lambda_1 \int_{outside(\Gamma)} \frac{(z-c_1)^2}{c_1^2} dxdy + \lambda_2 \int_{inside(\Gamma)} \frac{(z-c_2)^2}{c_2^2} dxdy$$

and μ, λ_1, λ_2 are constants and are used for assigning different weights.

Here for a discrete image z, the new model may be explained as follows. Denoting the image intensity at position (i,j) as $z_{i,j}$, the variance defined by

$$Var(z) = \frac{1}{N} \sum_{i,j} \Big(z_{i,j} - Mean(z) \Big)^2,$$

where $Mean(z)$, denoting the mean intensity of a given image, is previously used in the BC model as the fidelity term. The COV is defined as:

$$CoV^2 = \frac{Var(z)}{\Big(Mean(z) \Big)^2}$$

The value of CoV is higher in areas where there are edges than the areas which are uniform [17, 21]. It means that a higher value indicates that pixels belong to the edges and a small value indicates that the pixels belong to the uniform region. The properties of CoV [17, 21] indicate that it can be used as a fitting term as well as a good region detector. The experimental results using COV as fidelity term to modify the CV model show that the converged contour tends to be next the initial contour. We use COV to detect non-spurious objects near an initial contour.

Thus the level set formulation for (4) becomes

$$\begin{aligned} F(\phi, c_1, c_2) &= \mu \int_\Omega d(x,y) g(|\nabla z|) \delta(\phi) |\nabla \phi| dxdy + \lambda_1 \int_\Omega \frac{(z(x,y) - c_1)^2}{c_1^2} H(\phi) dxdy \\ &\quad + \lambda_2 \int_\Omega \frac{(z(x,y) - c_2)^2}{c_2^2} (1 - H(\phi)) dxdy, \end{aligned}$$

and a modified minimization problem from using H_ϵ and δ_ϵ:

$$\min_{\phi, c_1, c_2} F_\epsilon(\phi, c_1, c_2),$$

where

$$\begin{aligned} F_\epsilon(\phi, c_1, c_2) &= \mu \int_\Omega d(x,y) g(|\nabla z|) \delta_\epsilon(\phi) |\nabla \phi| dxdy + \lambda_1 \int_\Omega \frac{(z(x,y) - c_1)^2}{c_1^2} H_\epsilon(\phi) dxdy \\ &+ \lambda_2 \int_\Omega \frac{(z(x,y) - c_2)^2}{c_2^2} (1 - H_\epsilon(\phi)) dxdy. \end{aligned}$$

Keeping ϕ fixed and minimizing $F_\epsilon(\phi, c_1, c_2)$ with respect to c_1 and c_2, we have

$$c_1(\phi) = \frac{\int_\Omega z^2(x,y) H_\epsilon(\phi) dxdy}{\int_\Omega z(x,y) H_\epsilon(\phi) dxdy}, \tag{4}$$

and

$$c_2(\phi) = \frac{\int_\Omega z^2(x,y) (1 - H_\epsilon(\phi)) dxdy}{\int_\Omega z(x,y) (1 - H_\epsilon(\phi)) dxdy}. \tag{5}$$

Now keeping c_1, c_2 fixed and minimizing F_ϵ with respect to ϕ yields the following Euler-Lagrange equation for ϕ:

$$\begin{cases} \delta_\epsilon(\phi) \Big[\mu \mathrm{div}\Big(G(x,y) \frac{\nabla \phi}{|\nabla \phi|} \Big) \\ \qquad - \lambda_1 \dfrac{(z(x,y) - c_1)^2}{c_1^2} + \lambda_2 \dfrac{(z(x,y) - c_2)^2}{c_2^2} \Big] = 0 & \text{in } \Omega, \\ \dfrac{G(x,y) \delta_\epsilon(\phi)}{|\nabla \phi|} \dfrac{\partial \phi}{\partial \vec{n}} = 0 & \text{on } \partial\Omega, \end{cases} \tag{6}$$

where $G(x,y) = d(x,y) g(|\nabla z|)$.

Remark 3.1 *Denominators in (4) and (5) can be zero in situations where we need to segment an object/region having zero value. For such cases we can obtain the values of* c_1 *and* c_2 *as follows,*

$$c_1(\phi) = \frac{\int_\Omega z^2(x,y) H_\epsilon(\phi) dxdy}{\int_\Omega z(x,y) H_\epsilon(\phi) dxdy + \gamma}, \;\; c_2(\phi) = \frac{\int_\Omega z^2(x,y) (1 - H_\epsilon(\phi)) dxdy}{\int_\Omega z(x,y) (1 - H_\epsilon(\phi)) dxdy + \gamma},$$

where γ *is a small positive real number and similarly we may replace* c_l^2 *by* $c_l^2 + \gamma$ *in (6).*

We now add a balloon term $\alpha G(x,y)|\nabla\phi|$ to speed up the convergence of the evolution equation as done in [3]. Thus we get

$$\begin{aligned}\frac{\partial\phi}{\partial t} &= \delta_\epsilon(\phi)\Big[\mu\nabla.\Big(G(x,y)\frac{\nabla\phi}{|\nabla\phi|}\Big) - \lambda_1\frac{(z(x,y)-c_1)^2}{c_1^2} \\ &+ \lambda_2\frac{(z(x,y)-c_2)^2}{c_2^2} + \alpha G(x,y)|\nabla\phi|\Big], \quad in\ \Omega \\ \phi(t,x,y) &= \phi_0(x,y), \quad in\ \Omega.\end{aligned} \tag{7}$$

The existence of ϕ can be proved along similar lines to [11].

4 Numerical Methods

We present two numerical methods for solving nonlinear parabolic partial differential equation (7).

4.1 Semi implicit-method

First we write the PDE (7) in a self adjoint form

$$\frac{\partial\phi}{\partial t} = \mu\delta_\epsilon(\phi)\nabla\Big(G(x,y)\frac{\nabla\phi}{|\nabla\phi|}\Big) + f(x,y),$$

i.e.

$$\frac{\partial\phi}{\partial t} = \mu\delta_\epsilon(\phi(x,y))\Big[G(x,y)\nabla.\Big(\frac{\nabla\phi}{|\nabla\phi|}\Big) + \nabla G(x,y).\Big(\frac{\nabla\phi}{|\nabla\phi|}\Big)\Big] + f(x,y), \tag{8}$$

where

$$\begin{aligned}f(x,y) = \mu\delta_\epsilon(\phi)\Big[&- \lambda_1\frac{(z(x,y)-c_1)^2}{c_1^2} + \lambda_2\frac{(z(x,y)-c_2)^2}{c_2^2}\Big] \\ &+ \alpha G(x,y)|\nabla\phi|.\end{aligned}$$

Now using the following differences given by,

$$\begin{aligned}\Delta_-^x(\phi_{i,j}) &= \phi_{i,j} - \phi_{i-1,j}, \qquad \Delta_+^x(\phi_{i,j}) = \phi_{i+1,j} - \phi_{i,j} \\ \Delta_-^y(\phi_{i,j}) &= \phi_{i,j} - \phi_{i,j-1}, \qquad \Delta_+^y(\phi_{i,j}) = \phi_{i,j+1} - \phi_{i,j}\end{aligned}$$

and a semi implicit scheme, the discretized form of the above equation is:

$$\begin{aligned}\frac{\phi_{i,j}^{n+1}-\phi_{i,j}^n}{\triangle t} &= \mu\delta_\epsilon(\phi_{i,j}^n)G_{i,j}\Big[\frac{1}{h_1^2}\triangle_-^x\Big(\frac{\triangle_+^x\phi_{i,j}^{n+1}}{\sqrt{(\triangle_+^x\phi_{i,j}^n/h_1)^2 + (\triangle_+^y\phi_{i,j}^n/h_2)^2}}\Big)\Big] \\ &+ \mu\delta_\epsilon(\phi_{i,j}^n)G_{i,j}\frac{1}{h_2^2}\triangle_-^y\Big(\frac{\triangle_+^y\phi_{i,j}^{n+1}}{\sqrt{(\triangle_+^x\phi_{i,j}^n/h_1)^2} + (\triangle_+^y\phi_{i,j}^n/h_2)^2}\Big) \\ &+ \mu\frac{\delta_\epsilon(\phi_{i,j}^n)}{|\nabla\phi_{i,j}^n|}\Big(\frac{1}{h_1^2}\triangle_+^x G(x,y)\triangle_+^x\phi_{i,j}^{n+1}\Big) + \frac{\mu\delta_\epsilon(\phi_{i,j}^n)}{|\nabla\phi_{i,j}^n|}\Big(\frac{1}{h_2^2}\triangle_+^y G(x,y)\triangle_+^y\phi_{i,j}^{n+1}\Big) + f_{i,j}.\end{aligned}$$

Using $h_1 = h_2 = 1$ (i.e. absorb h_1 and h_2 into the parameter μ), we get

$$\begin{aligned}\frac{\phi_{i,j}^{n+1} - \phi_{i,j}^{n}}{\triangle t} &= \mu\delta_\epsilon(\phi_{i,j}^n)G_{i,j}\Big[(\phi_{i+1,j}^{n+1} - \phi_{i,j}^{n+1})C_{i,j} - (\phi_{i,j}^{n+1} - \phi_{i-1,j}^{n+1})C_{i-1,j} \\ &+ (\phi_{i,j+1}^{n+1} - \phi_{i,j}^{n+1})C_{i,j} - (\phi_{i,j}^{n+1} - \phi_{i,j-1}^{n+1})C_{i,j-1}\Big] \\ &+ \frac{\mu\delta_\epsilon(\phi_{i,j}^n)}{|\nabla\phi_{i,j}^n|}\Big[\triangle_+^x G(x,y)(\phi_{i+1,j}^{n+1} - \phi_{i,j}^{n+1}) + \triangle_+^y G(x,y)(\phi_{i,j+1}^{n+1} - \phi_{i,j}^{n+1})\Big] + f_{i,j},\end{aligned} \tag{9}$$

where

$$\begin{aligned}C_{i,j} &= \frac{1}{\sqrt{(\Delta_+^x\phi_{i,j}^n)^2 + (\Delta_+^y\phi_{i,j}^n)^2}} \\ C_{i-1,j} &= \frac{1}{\sqrt{(\Delta_+^x\phi_{i-1,j}^n)^2 + (\Delta_+^y\phi_{i-1,j}^n)^2}} \\ C_{i,j-1} &= \frac{1}{\sqrt{(\Delta_+^x\phi_{i,j-1}^n)^2 + (\Delta_+^y\phi_{i,j-1}^n)^2}}.\end{aligned}$$

As the coefficients $C_{i-1,j}$, $C_{i,j}$ and $C_{i,j-1}$ are freezed at the nth iteration, equation (9) defines a linear system of equations which can be solved by an iterative method. To speed the solution we shall develop AOS method as done in [16, 25, 26] to solve the PDE (7).

4.2 An Additive Operator Splitting Method

The above introduced semi-implicit method, though stable with respect to Δt, can be expensive to apply if the spatial dimension ≥ 2. Related to the famous ADI (alternating direction implicit methods [9]), the AOS scheme [16, 25] splits the 2-dimensional spatial operator into a sum of two one dimensional space discretizations so that the resulting linear system can be efficiently solved by applying two times the Thomas algorithm; other splitting methods (e.g. multiplicative type) may also be considered. Rewrite the PDE (8) in the form

$$\begin{aligned}\frac{\partial\phi}{\partial t} &= \mu\delta_\epsilon(\phi)\nabla(F\nabla\phi) + f \\ &= \mu\delta_\epsilon(\phi)\Big(\partial_x(F\partial_x\phi) + \partial_y(F\partial_y\phi)\Big) + f,\end{aligned}$$

where $F = \frac{G}{|\nabla\phi|}$. Therefore we consider the first one-dimensional problem in x-direction:

$$\frac{\phi_{i,j}^{n+1} - \phi_{i,j}^{n}}{\triangle t} = \mu\delta_\epsilon(\phi)\Big(F_{i+1/2,j}^n(\phi_{i+1,j}^{n+1} - \phi_{i,j}^{n+1}) - F_{i-1/2,j}^n(\phi_{i,j}^{n+1} - \phi_{i-1,j}^{n+1})\Big) + f_{i,j}$$

i.e.,

$$\phi_{i,j}^{n+1} = \phi_{i,j}^n + \mu\triangle t\Big(c_1\phi_{i+1,j}^{n+1} - c_2\phi_{i,j}^{n+1} + c_3\phi_{i-1,j}^{n+1}\Big) + f_{i,j}, \tag{10}$$

where

$$\begin{aligned} c_1 &= \delta_\epsilon(\phi)\frac{F^n_{i,j} + F^n_{i+1,j}}{2}, \\ c_2 &= \delta_\epsilon(\phi)\frac{F^n_{i-1,j} + 2F^n_{i,j} + F^n_{i+1,j}}{2}, \\ c_2 &= \delta_\epsilon(\phi)\frac{F^n_{i,j} + F^n_{i-1,j}}{2}. \end{aligned}$$

After we solve the system of equations (10) in the x-direction, we then solve a similar system in y-direction before averaging the two solutions:

$$\begin{aligned} (I - 2\Delta t A_l(\Phi^n))\Phi^{n+1}_l &= f^n, for\ l = 1, 2, \\ \text{and } \Phi^{n+1}_l &= \frac{1}{2}\sum_{l=1}^{2}\Phi^{n+1}_l, \end{aligned}$$

where I is the identity matrix and $A_l\ for\ l = 1, 2$ a tridiagonal matrix. AOS scheme uses 1-D semi implicit scheme in spatial directions independently, so AOS scheme is absolutely stable. Both computational and storage effort is linear in the number of pixels. Other methods for solution of this PDE is the Additive-Multiplicative Operator Splitting (AMOS) schemes [4] and Multigrid method can also be used to solve the above PDE.

5 Experimental Results

In this section some simulation results are given. The experiments show that the new method CSM preserves advantages of the BC method such as robustness in terms of number of iterations, CPU time, segmenting noisy images. It has also been observed that the CSM performs better when segmenting images with fuzzy edges, images with homogeneous overlapping regions. The comparison below verifies this discussion. For the sake of comprehensive comparisons, we also include the Gout model in these experiments. For clarity, we shall denote by

M-1 — the Gout model
M-2 — the BC model and
M-3 — the proposed CSM.

Below we give the original images along with comparison results of these three methods. We begin with some simple examples where M-1, M-2 and M-3 work well. Then we give some more examples to show that M-3 has far better performance than M-1, M-2. In both M-2 and M-3, we use $\lambda_1 = \lambda_2 = \lambda$. In each of the following figures, the performance of M-1, M-2 and proposed M-3 can be seen in row first, second and third respectively. The first row shows the performance of M-1, the second row shows performance of M-2 and the third row shows performance of M-3. The first column shows the original image with initial contours. The second column displays the intermediate situations of active contour of each model. The third column reveals the final solution in each model and the fourth

column displays the segmented version of the final solution for the sake of convenience in deep observations.

The behavior of M-2 can be seen in figures 2(g), 3(g), 4(g), 5(g) up to 8(g). On the other hand much of the experiments reveal the unpredictable behavior of M-1 as it mainly depends on edge detector function only. In figures 2(c), 4(c) and 6(c) it can be seen that instead of completing its selective segmentation task, M-1 started detection of other undesired region/object. In contrast with M-1, M-2, the best performance of M-3 can be seen from the experiments. The experiments also exhibit that M-3 is best in accurate and fast detection and successful in the images in which these two models are unable to work.

In figure 2 the original image with initial contour is given. Its clear from figures 2(c), 2(d), 2(g) and 2(h) that M-1 and M-2 are unable to detect the region of interest. On the other hand successful results of M-3 can be seen in 2(k) and 2(l). In figure 2(a) the original image with initial contour is displayed. The figure 2(c) shows that M-1 detected the selected region in 1200 iterations where as figure 2(k) displays that M-3 detected the same region in only 35 iterations. On the other hand the performance of M-2 can easily be interpreted in figure 2(g). In figure 4(a) a medical image with initial contour is displayed. The accuracy of detection of M-2 and M-3 is clearly visible by observing figures 4(g), 4(h), 4(k) and 4(l).

The figure 5 exhibits real breast image in which we wish to detect a white region. Although It can be seen in 5(c) and 5(d) that M-1 detected the desired region but it should also be noted that it took 800 iterations and consumed our precious time to search an ideal initial contour for this model. An ideal initial contour for M-1 is a contour to be selected almost on the boundary of an object/region of interest. It can be seen clearly in figures 2(a), 3(a), 5(a), 6(a) and 7(a), that an ideal initial contour is provided to M-1, but still the results are devastating. In contrast with M-1, it can be easily observed in 2(i), 3(i), 4(i), 5(i), 6(i), 7(i), 8(i) and 9(i) that M-3 gives best results without demanding an ideal initial contour. The figure 6 displays a synthetic image and the performance of all of the three models. The proposed M-3 successfully detects a selected region in synthetic image and can be viewed as figure 6(k). The figures 6(c), 6(g) are displaying that M-1 and M-2 are unable to detect the selected object in the given image.

The figure 7 exhibits a real eye image and the performance of all of the three models by detecting a black region. The figure 7(k) shows the successful detection by M-3 of the desired region. Figures 7(c) and 7(g) show that M-1 and M-2 are unable to complete the tasks. A real heart image can viewed in figure 8. Successful detection of selected portion in real heart image by the proposed M-3 can be seen in figure 8(k), where as figures 8(g) and 8(c) show inaccurate detection of M-1 and M-2. In figure 9 a real abdominal image can be viewed. Using that real abdominal image, the detected results of the three models are displayed. With simple observation of figures 9(k), 9(g) and 9(c) it can be easily interpreted that M-3 successfully complete the task, whereas the remaining two models M-1 and M-2 are unable to complete the task. The figure 10 exhibits the performance of

M-3 in fog images. This idea can be extended to video segmentation to utilize it in many applications.

In summary, it has been observed from the experiments that, while performing selective segmentation on the challenging images having nearly equal intensity regions or fuzzy edges, the performance of M-2 is less effective, as in such cases it is often observed that the active contour crosses the boundary of an object of interest in the image and therefore the existing model is unable in detecting the actual boundary and consequently the region of interest in the image. In contrast, the proposed new M-3 outperforms all existing methods.

6 Conclusions

In this paper a new active contour model for selective image segmentation based on coefficient of variation is presented. This model works better in segmenting images having objects whose edges are not prominent, than previous work. It has ability of detecting objects with overlapping boundaries having homogeneous intensities and also can detect objects having non homogeneous intensities. In future we plan to develop fast multigrid methods for solution of differential equations arisen from minimization of the model and will extend these results to segmenting 3D images.

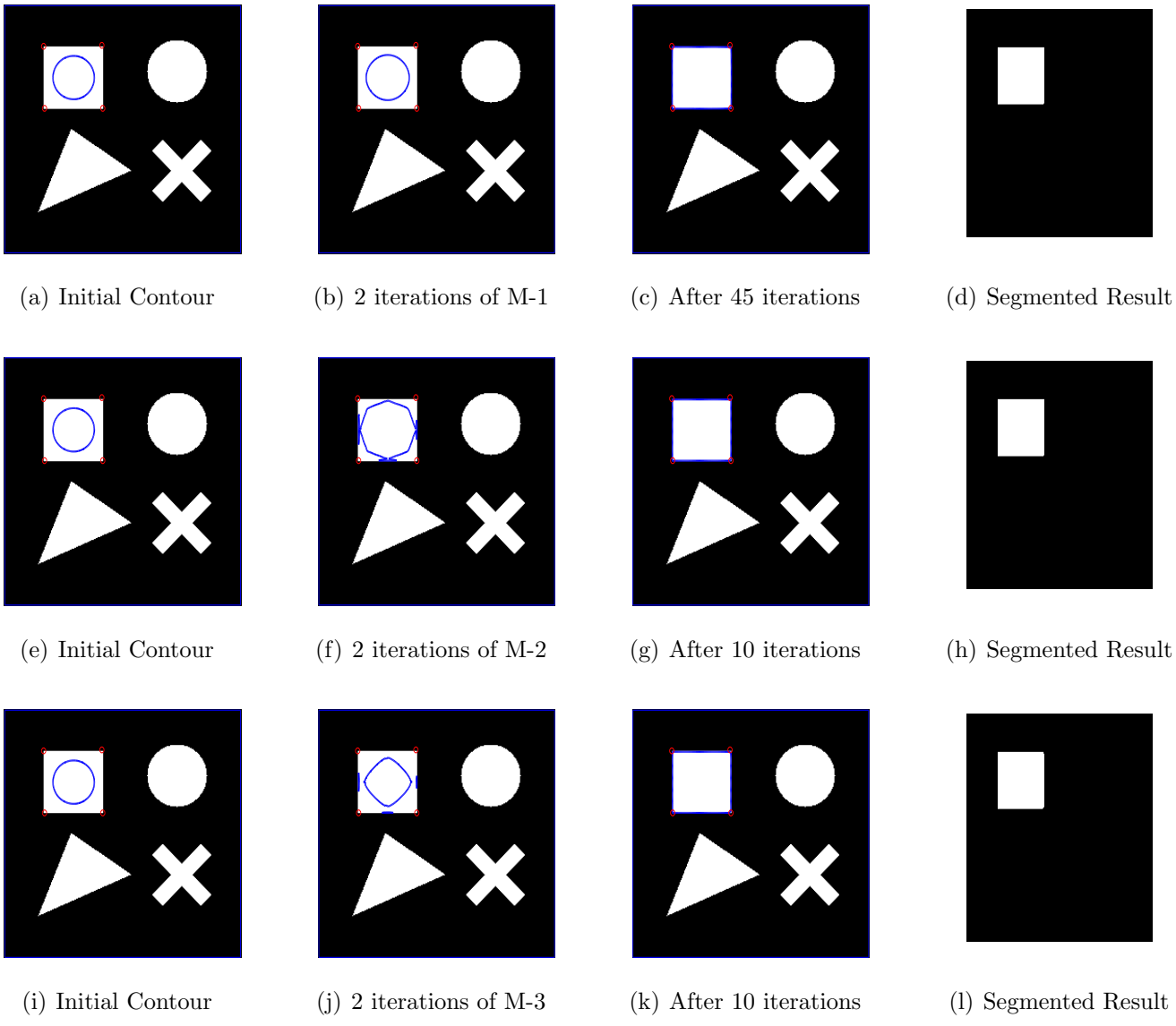

(a) Initial Contour (b) 2 iterations of M-1 (c) After 45 iterations (d) Segmented Result

(e) Initial Contour (f) 2 iterations of M-2 (g) After 10 iterations (h) Segmented Result

(i) Initial Contour (j) 2 iterations of M-3 (k) After 10 iterations (l) Segmented Result

Figure 1: Simple example of segmenting synthetic image, where M-1, M-2 and M-3 have completed the task. M-1 took 19 seconds and both M-2 and M-3 took 4 seconds to complete the task. For M-2 and M-3 model parameters used are: $\lambda = 1$, $\mu = 256^2/400$ and for all the three models $\alpha = -0.1$. The performance of M-1, M-2 and M-3 model can be seen in row first, second and third respectively.

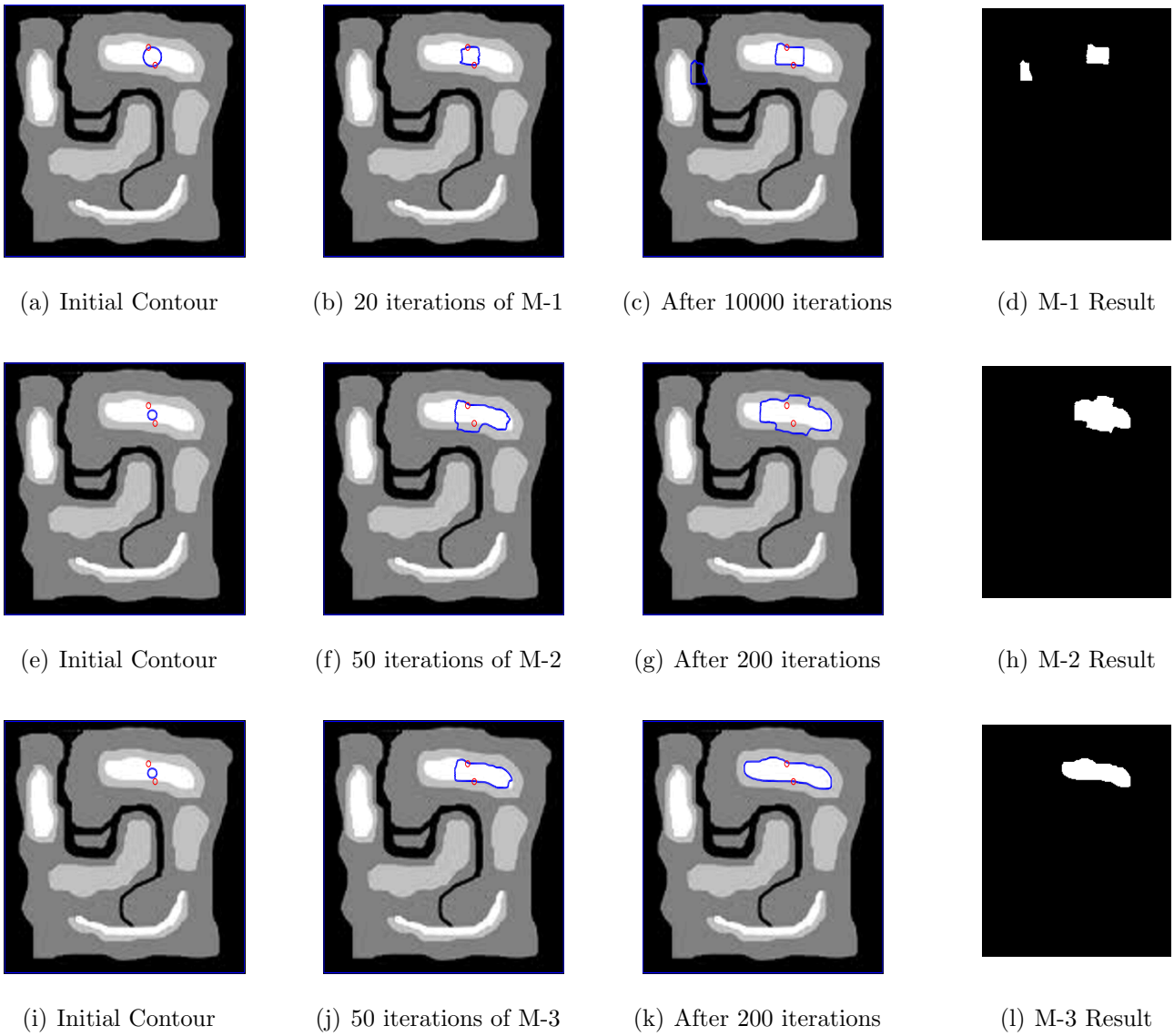

(a) Initial Contour (b) 20 iterations of M-1 (c) After 10000 iterations (d) M-1 Result

(e) Initial Contour (f) 50 iterations of M-2 (g) After 200 iterations (h) M-2 Result

(i) Initial Contour (j) 50 iterations of M-3 (k) After 200 iterations (l) M-3 Result

Figure 2: A comparison of M-1, M-2 and the proposed M-3 on segmenting a synthetic image. M-3 successfully detected the selected region. For M-3 model parameters used are: $\lambda = 20$, $\mu = 256^2/5000$ and $\alpha = 0$. Figures 2(c), 2(d), 2(g) and 2(h) are displaying that M-1 and M-2 are unable to detect the selected object in the given image.

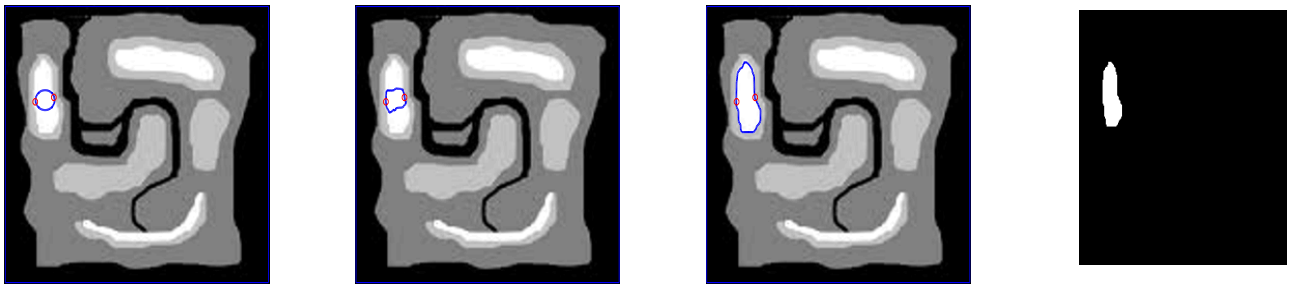

(a) Initial Contour (b) 20 iterations of M-1 (c) After 1200 iterations (d) M-1 Result

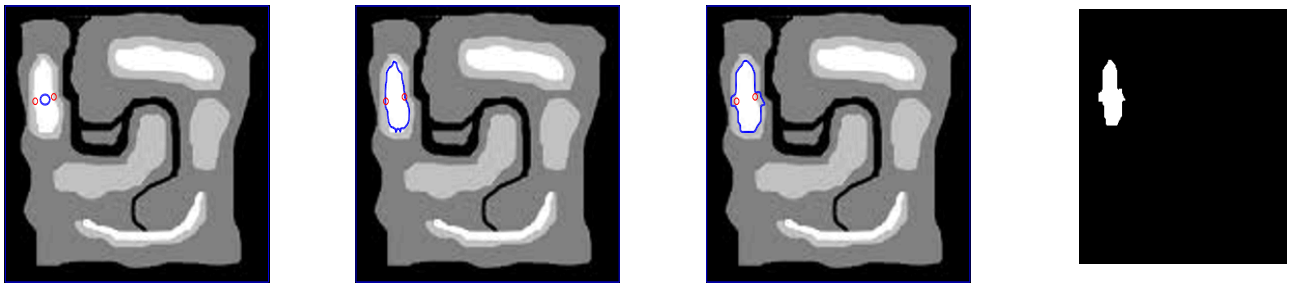

(e) Initial Contour (f) 30 iterations of M-2 (g) After 200 iterations (h) M-2 Result

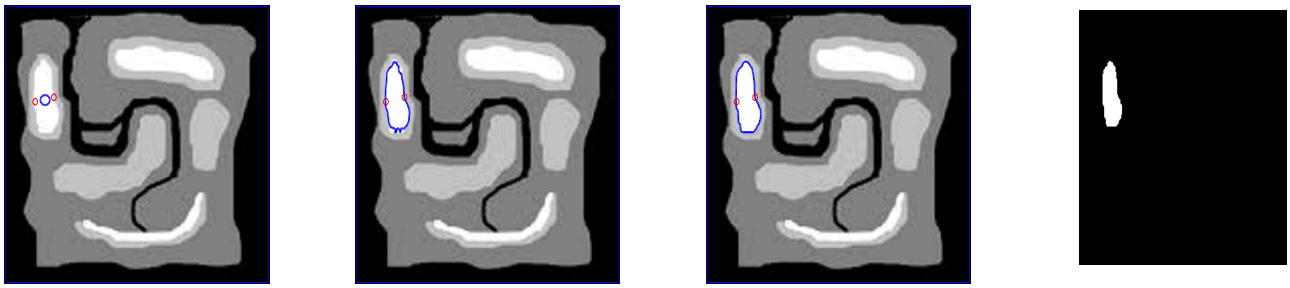

(i) Initial Contour (j) 20 iterations of M-3 (k) After 35 iterations (l) M-3 Result

Figure 3: Comparison of M-1 in figure 3(c) which took 1200 iterations to converge final solution with M-3 in figure 3(k) converging to final solution in only 35 iterations. By observing the figures 3(g), 3(h) the comparison between M-2 (failing this example) and M-3 is simple. For M-3, the model parameters used are: $\lambda = 15$, $\mu = 256^2/5000$ and $\alpha = 0$.

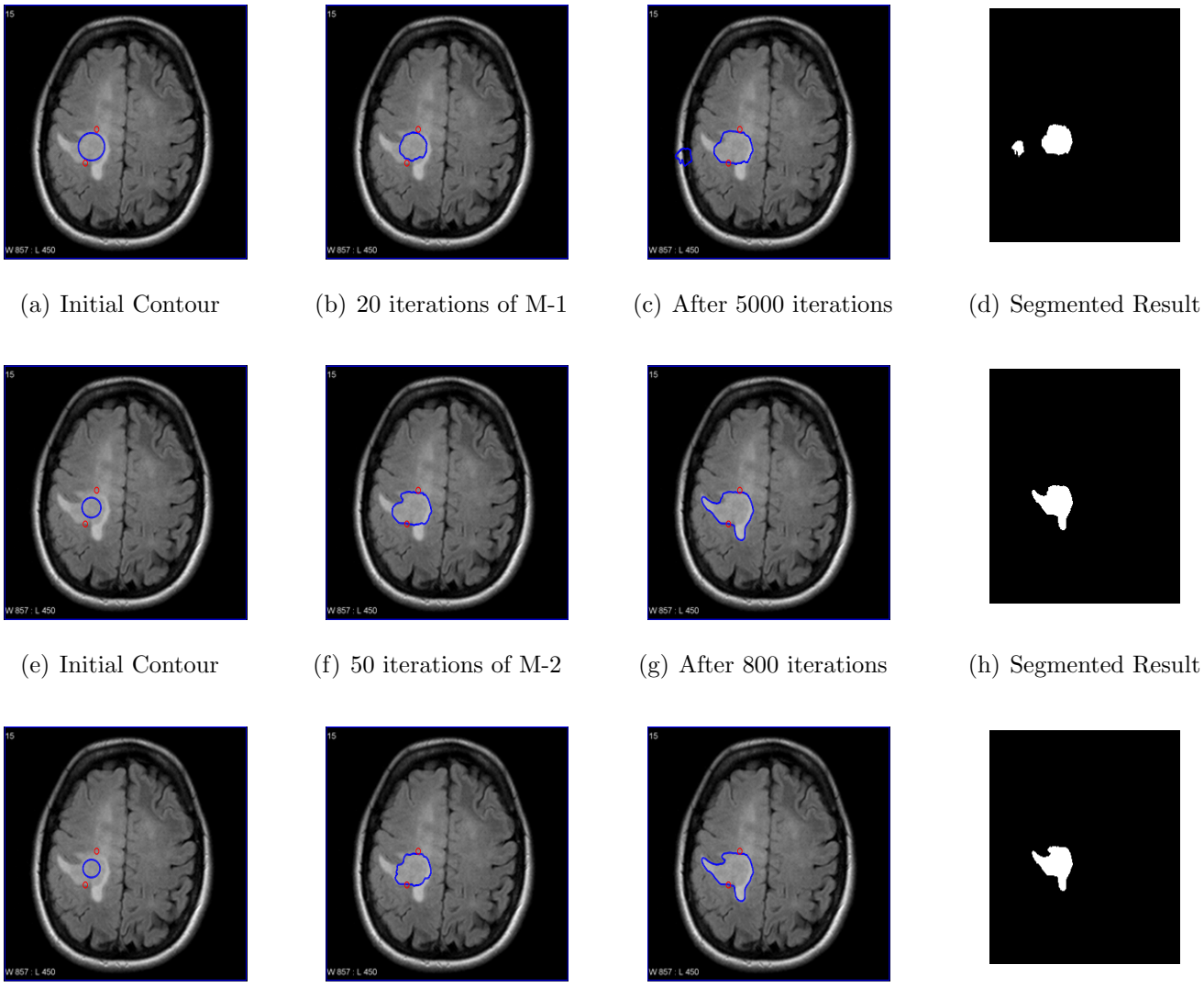

(a) Initial Contour (b) 20 iterations of M-1 (c) After 5000 iterations (d) Segmented Result

(e) Initial Contour (f) 50 iterations of M-2 (g) After 800 iterations (h) Segmented Result

(i) Initial Contour (j) 50 iterations of M-3 (k) After 800 iterations (l) Segmented Result

Figure 4: The quality of detection of M-2 and M-3 can easily be compared by observing figures 4(g), 4(h), 4(k) and 4(l). Figure 4(c) reveals that M-1 (failing this example) is unable to complete the task. For M-3 parameters used are: $\lambda = 4$, $\mu = 256^2/10000$ and $\alpha = 0$.

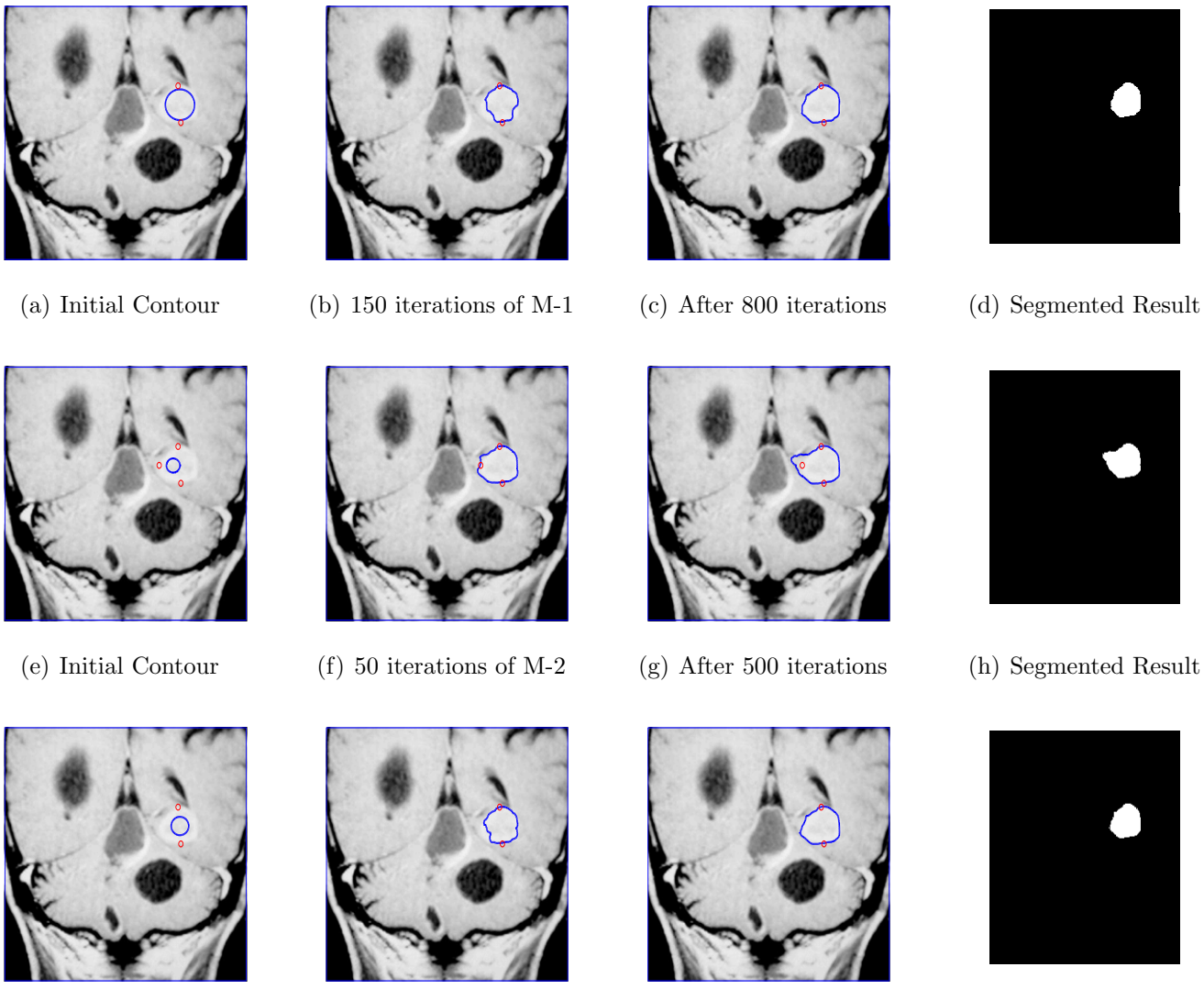

(a) Initial Contour (b) 150 iterations of M-1 (c) After 800 iterations (d) Segmented Result

(e) Initial Contour (f) 50 iterations of M-2 (g) After 500 iterations (h) Segmented Result

(i) Initial Contour (j) 50 iterations of M-3 (k) After 380 iterations (l) Segmented Result

Figure 5: M-3 Successfully detects a white spot in real breast image. In figure 5(g) its clear that active contour of M-2 has crossed the boundary of the region of interest. For M-3 parameters used are: $\lambda = 20$, $\mu = 256^2/5000$ and $\alpha = 0$.

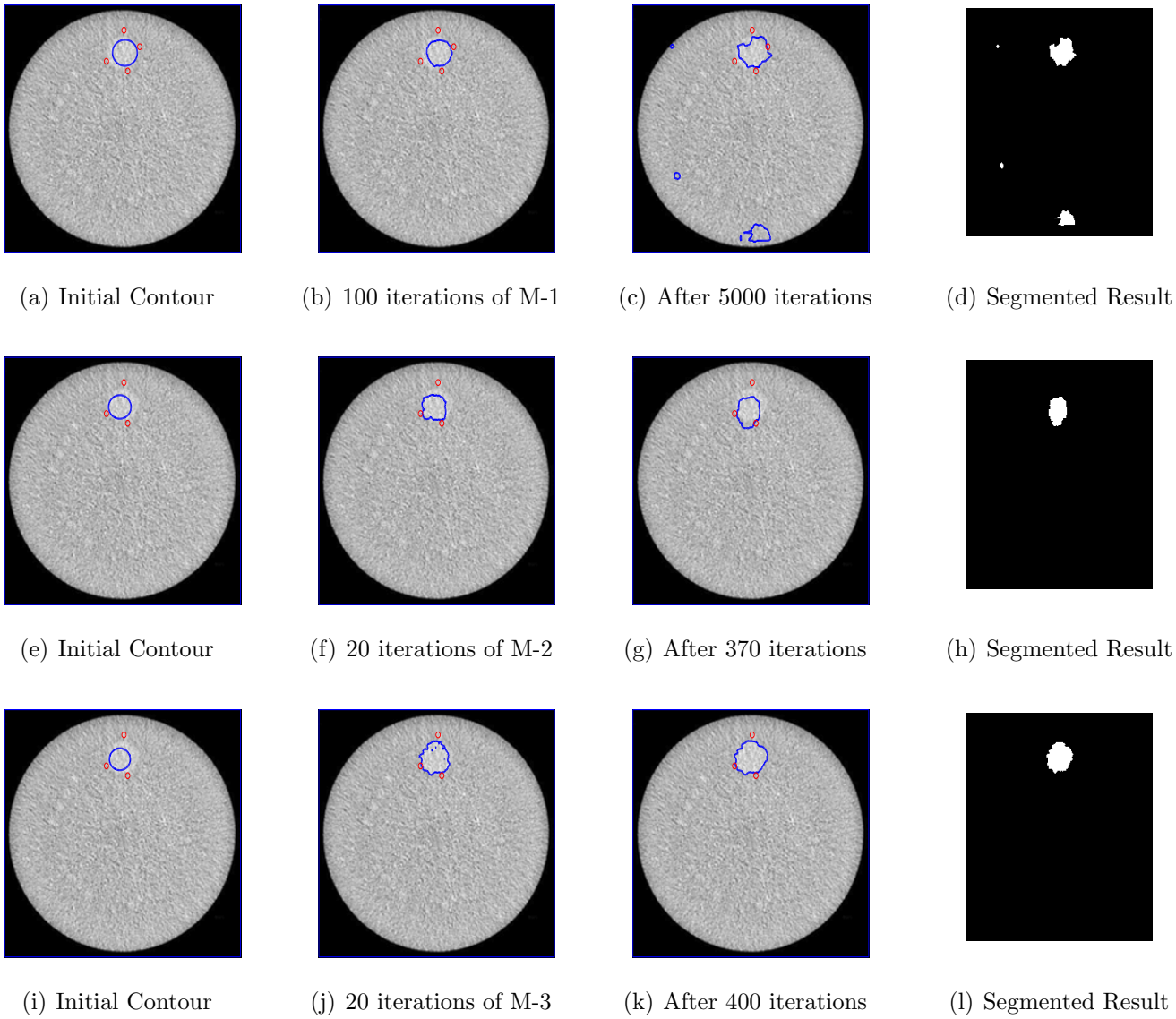

(a) Initial Contour (b) 100 iterations of M-1 (c) After 5000 iterations (d) Segmented Result

(e) Initial Contour (f) 20 iterations of M-2 (g) After 370 iterations (h) Segmented Result

(i) Initial Contour (j) 20 iterations of M-3 (k) After 400 iterations (l) Segmented Result

Figure 6: Successful detection of M-3 of selected region in synthetic image can be viewed in figure 6(k). Figures 6(c), 6(g) are displaying that M-1 and M-2 are unable to detect the selected object in the given image. For M-3 parameters used are: $\lambda = 150$, $\mu = 256^2/4000$ and $\alpha = 0$

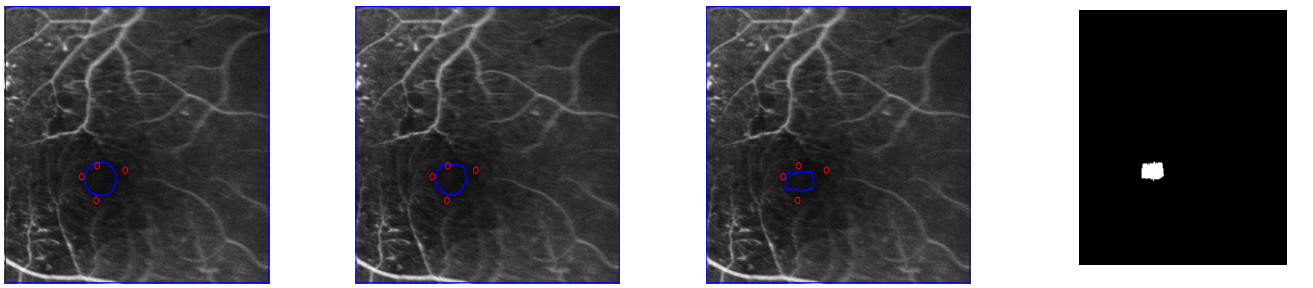

(a) Initial Contour (b) 100 iterations of M-1 (c) After 10000 iterations (d) Segmented Result

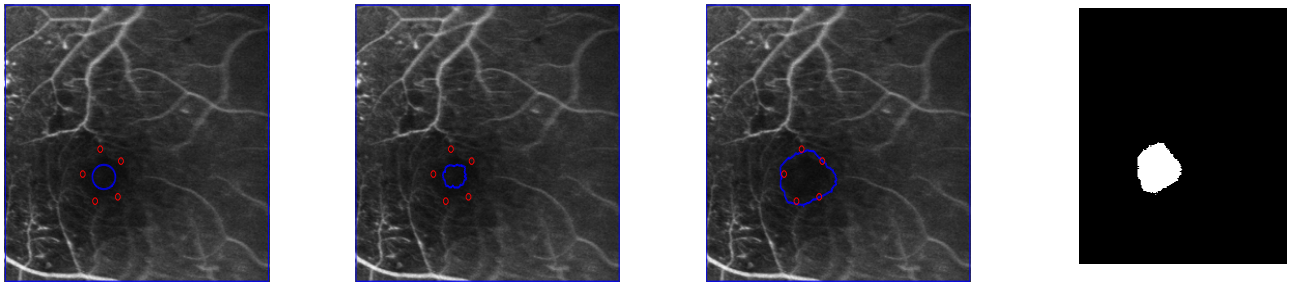

(e) Initial Contour (f) 20 iterations of M-2 (g) After 1000 iterations (h) Segmented Result

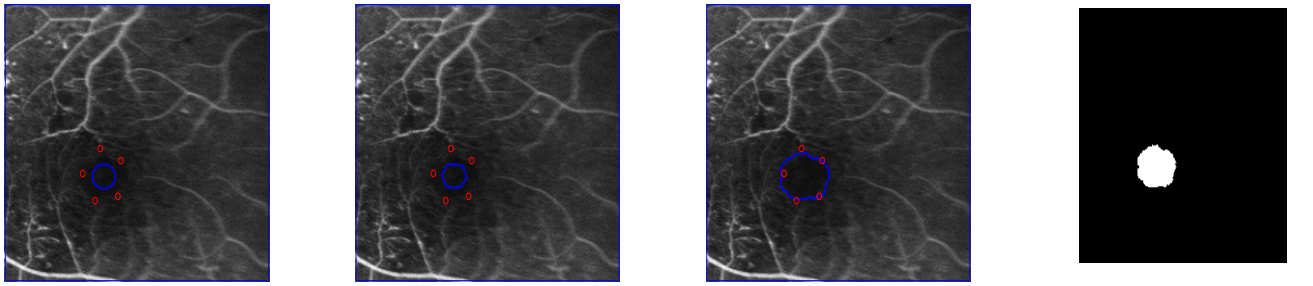

(i) Initial Contour (j) 20 iterations of M-3 (k) After 1200 iterations (l) Segmented Result

Figure 7: These experiments exhibit the performance of all of the three models by detecting a black region in real eye image. Figure 7(k) shows the successful detection by M-3 of the desired region. Figures 7(c) and 7(g) show that M-1 and M-2 are unable to complete the tasks. For M-3 parameters used are: $\lambda = 0.4$, $\mu = 256^2/20000$ and $\alpha = -0.00125$.

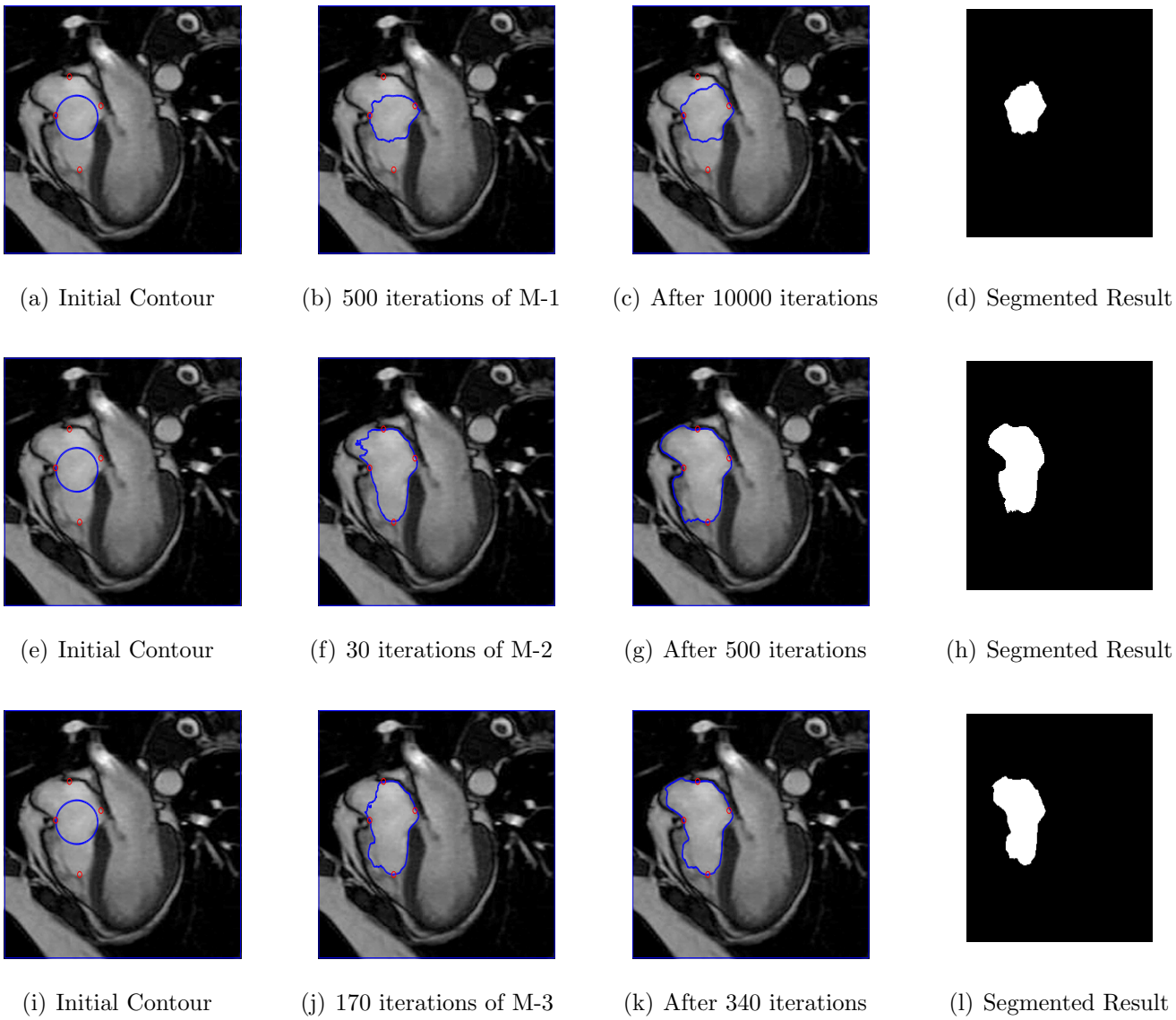

(a) Initial Contour (b) 500 iterations of M-1 (c) After 10000 iterations (d) Segmented Result

(e) Initial Contour (f) 30 iterations of M-2 (g) After 500 iterations (h) Segmented Result

(i) Initial Contour (j) 170 iterations of M-3 (k) After 340 iterations (l) Segmented Result

Figure 8: Successful detection of selected portion in real heart image by the proposed M-3 can be seen in figure 8(k). For M-3 parameters used are: $\lambda = 20$, $\mu = 256^2/5000$ and $\alpha = 0$. In contrast with M-3, the uncompleted tasks by M-1 and M-2 can also be seen clearly in 8(c) and 8(g).

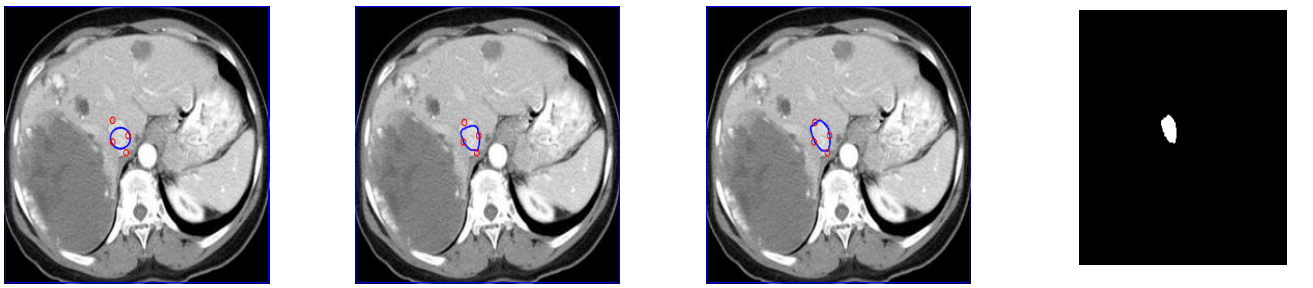

(a) Initial Contour (b) 500 iterations of M-1 (c) After 10000 iterations (d) Segmented Result

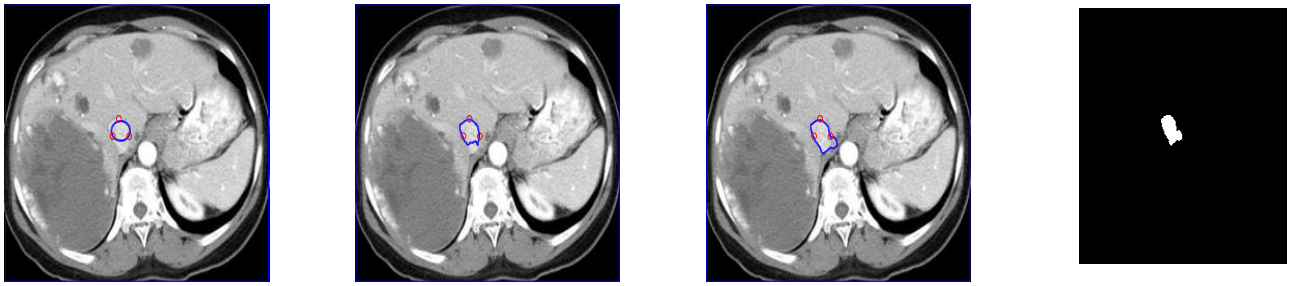

(e) Initial Contour (f) 14 iterations of M-2 (g) After 370 iterations (h) Segmented Result

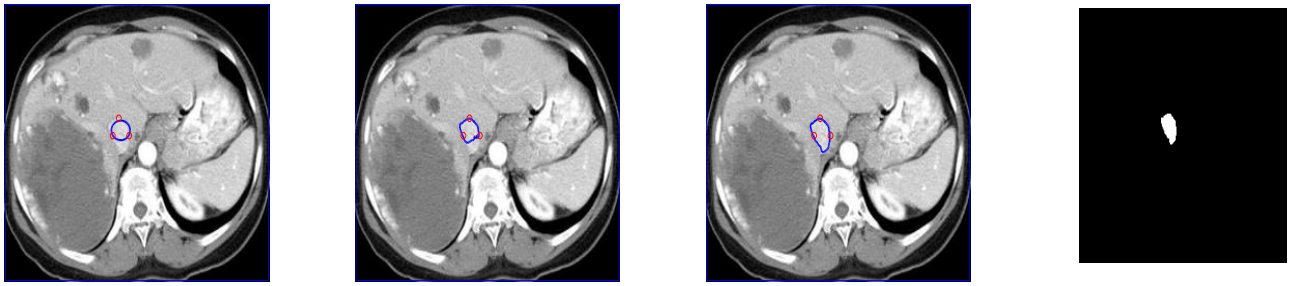

(i) Initial Contour (j) 60 iterations of M-3 (k) After 135 iterations (l) Segmented Result

Figure 9: Using this real abdominal image, the detected results of the three models are displayed. With simple observation of figures 9(k), 9(g) and 9(c) it can be easily interpreted that M-3 successfully completed the task. For M-3 parameters used are: $\lambda = 2$, $\mu = 256^2/1500$ and $\alpha = -0.01$.

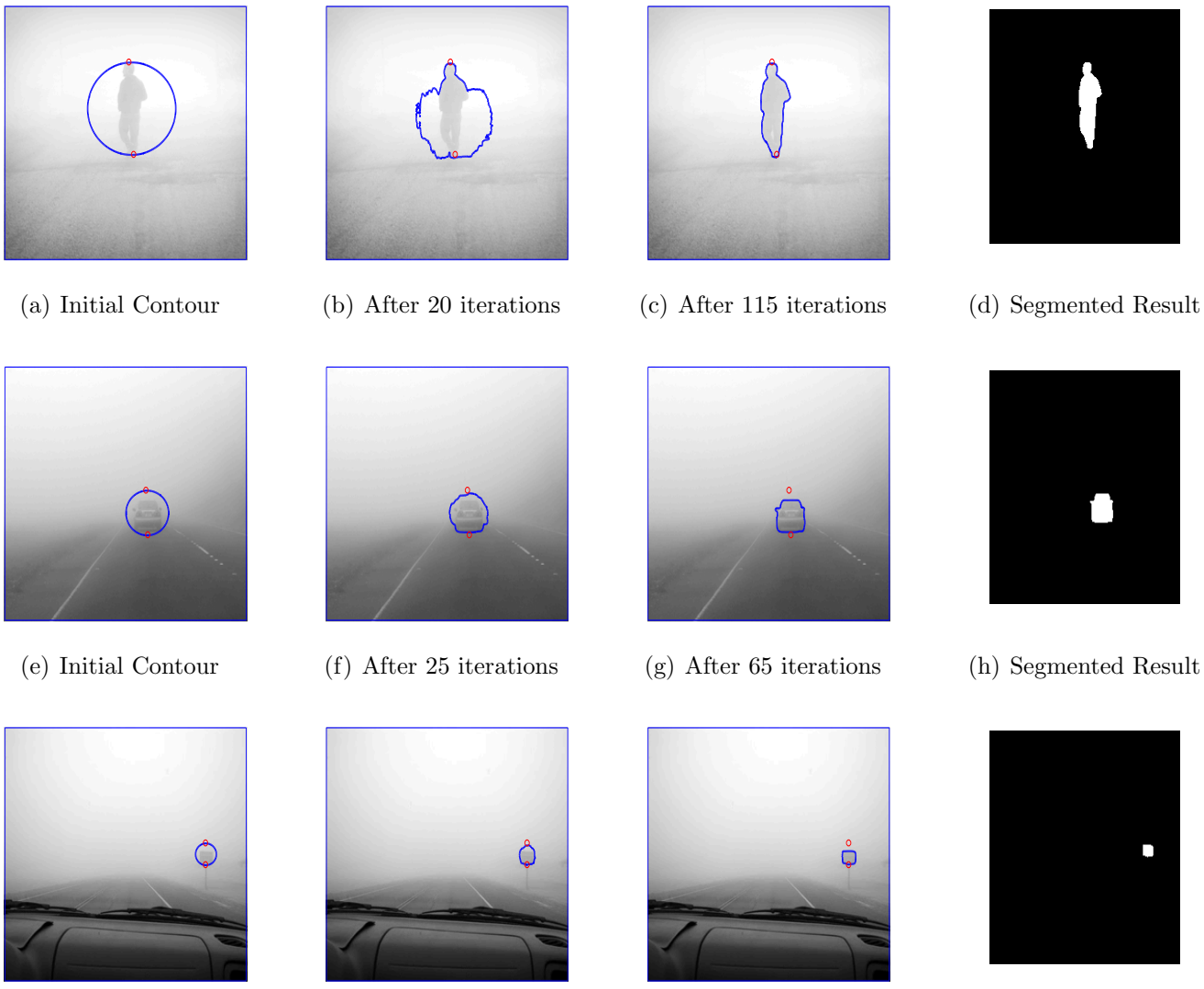

(a) Initial Contour (b) After 20 iterations (c) After 115 iterations (d) Segmented Result

(e) Initial Contour (f) After 25 iterations (g) After 65 iterations (h) Segmented Result

(i) Initial Contour (j) After 2 iterations (k) After 10 iterations (l) Segmented Result

Figure 10: Performance of M-3 in fog images. For fog man image (c) M-3 parameters used are: $\lambda = 0.01$, $\mu = 5$ and $\alpha = -0.00000151$, for figure (g) $\lambda = 0.01$, $\mu = 0.5$ and $\alpha = 0.00151$ and for figure (k) $\lambda = 0.5$, $\mu = 2$ and $\alpha = -0.0007$.

References

[1] S. E. Ahmed. A pooling methodology for coefficient of variation. Sankhya: The Indian Journal of Statistics, 57(B1):57–75, 1995.

[2] R. Adams and L. Bischof. Seeded region growing. IEEE Trans. Pattern Analysis and-Machine Intelligence, 16(6):641-647, 1994.

[3] N. Badshah and K. Chen. Image Selective Segmentation under Geometrical Constraints Using an Active Contour Approach. Math. Comp., 7:759–778, 2010.

[4] D. Barash and R. Kimmel An Accurate Operator Splitting Scheme for Nonlinear Diffusion Filtering HP Laboratories Israel1 HPL-2000-48(R.1) August 1st, 2000

[5] V. Caselles, R. Kimmel and G. Sapiro. Geodesic active contours. International Jornal of Computer Vision, 22(1):61–79, 1997.

[6] T. F. Chan and L. A. Vese. Active contours without edges. IEEE Transactions on Image Processing, 10(2):266–277, 2001.

[7] K. Chen. Matrix Preconditioning Techniques and Applications. Cambridge University Press, 2005.

[8] L. D. Cohen. On active contour models and balloons. In Computer Vision, Graphics, and Image Processing: Image Understanding, 53(2):211–218.

[9] J. Douglas and H. H. Rachford. On the numerical solution of heat conduction problems in two and three space variables, Trans. Amer. Math. Soc., 82:421-439, 1956.

[10] C. Gout, C. L. Guyader and L. A. Vese. Segmentation under geometrical conditions with geodesic active contour and interpolation using level set method. Numerical Algorithms, 39:155-173, 2005.

[11] C. L. Guyader and C. Gout. Geodesic active contour under geometrical conditions theory and 3D applications. Numerical Algorithms, 48:105-133, 2008.

[12] M. Jeon, M. Alexander, W. Pedrycz, and N. Pizzi. Unsupervised hierarchical image segmentation with level set and additive operator splitting. PRL., 26(10):1461-1469, 2005.

[13] M. Kass, A. Witkin and D. Terzopoulos. Snakes: active Contours Models. International Jornal of Computer Vision, 1:321–331, 1988.

[14] Y. Leclerc. Region growing using the MDL principle, In: DAPPRA Image Understanding Workshop, 1990.

[15] Y. B. Li and J. S. Kim. Multiphase image segmentation using a phase-field model. Computers and Mathematics with Applications, 62:737–745, 2011.

[16] T. Lu, P. Neittaanmaki, and X. C. Tai. A parallel splitting up method and its application to Navier-Stokes equations Appl. Math. Lett., 4(2):25-29, 1991.

[17] M. Mora, C. Tauber, H. Batatia. Robust level set for heart cavities detection in ultrasound images Computers in Cardiology, 32:235-238, 2005.

[18] D. Mumford and J. Shah. Optimal approximation by piecewise smooth functions and associated variational problems. Communications on Pure Applied Mathematics, 42:577–685, 1989.

[19] S. Osher and R. Fedkiw Γ-Level Set Methods and Dynamic Implicit Surfaces, Springer Verlag, 2003 Lec. Notes Comp. Sci., 3708:499-506, 2005.

[20] S. Osher and J. A. Sethian. Fronts propagating with curvature-dependent speed: algorithms based on Hamilton-Jacobi formulations. J. Comput. Phys., 79(1):12–49, 1988.

[21] M. A. Schulze and Q. X. Wu. Nonlinear edge-preserving smoothing of synthetic aperture radar images. Proceedings of the New Zealand Image and Vision Computing '95 Workshop, pp.65– 70, 1995.

[22] J. A. Sethian Level set methods and fast marching methods. Evolving interfaces in Computational Geometry, Fluid Mechanics, Computer Vision and Material Science, Cambridge University Press, 1999.

[23] L. A. Vese and T. F. Chan. A multiphase level set framework for image segmentation using the Mumford and Shah model, Int. J. Computer Vision, 50(3):271-293, 2002.

[24] L. Vincent and Soille. Watersheds in Digital Spaces - an efficient algorithm based on immersion. IEEE Trans. Pattern Analysis and Machine Learning, 6:583-598, 1994.

[25] J. Weickert, B. M. ter Haar Romeny and M. A. Viergever. Efficient and reliable schemes for nonlinear diffusion filtering, IEEE Trans. Image Proc., 7:398-410, 1998.

[26] J. Weickert and G. Kuhne. Fast methods for implicit active contours models. In: Geometric Level SetMethods in Imaging, Vision, and Graphics, pp.43-58, 2003.

[27] Y. Yu and S. T. Acton. Edge detection in ultrasound imagery using the instantaneous coefficient of variation. IEEE Transactions On Image Processing 13(12):1640–1655, 2004.